FULL PAPER

Magnetic Resonance in Medicine 00:00–00 (2016)

Mitigation of B_1^+ Inhomogeneity Using Spatially Selective Excitation with Jointly Designed Quadratic Spatial Encoding Magnetic Fields and RF Shimming

Yi-Cheng Hsu,[1] Riccardo Lattanzi,[2] Ying-Hua Chu,[1] Martijn A. Cloos,[2] Daniel K. Sodickson,[2] and Fa-Hsuan Lin[1,3]*

Purpose: The inhomogeneity of flip angle distribution is a major challenge impeding the application of high-field MRI. We report a method combining spatially selective excitation using generalized spatial encoding magnetic fields (SAGS) with radiofrequency (RF) shimming to achieve homogeneous excitation. This method can be an alternative approach to address the challenge of B_1^+ inhomogeneity using nonlinear gradients.
Methods: We proposed a two-step algorithm that jointly optimizes the combination of nonlinear spatial encoding magnetic fields and the combination of multiple RF transmitter coils and then optimizes the locations, RF amplitudes, and phases of the spokes.
Results: Our results show that jointly designed SAGS and RF shimming can provide a more homogeneous flip angle distribution than using SAGS or RF shimming alone. Compared with RF shimming alone, our approach can reduce the relative standard deviation of flip angle by 56% and 52% using phantom and human head data, respectively.
Conclusion: The jointly designed SAGS and RF shimming method can be used to achieve homogeneous flip angle distributions when fully parallel RF transmission is not available.
Magn Reson Med 000:000–000, 2016. © 2016 International Society for Magnetic Resonance in Medicine.

Key words: 7T; RF inhomogeneity; nonlinear gradient; SAR; RF shimming; fast imaging

INTRODUCTION

High-field MRI can provide higher signal-to-noise ratio (1) and different contrasts (2) than low-field MRI, which can be exploited to improve spatial resolution or contrast-to-noise ratio without lengthening acquisition time (3). Yet imaging at high fields remains challenging due to the inhomogeneous flip angle distributions (4) caused by interference patterns between dielectric tissues and the radiofrequency (RF) fields, because the wavelength becomes comparable to the dimensions of the human body when B_0 is equal or higher than 3 T (5). In 3 T abdominal imaging, this effect can result in signal voids, which can be particularly severe (6). In head imaging, interference patterns typically result in a central region with large flip angles surrounded by a ring of low flip angles (i.e., "central brightening") (7). Such spatially varying flip angle distribution can result in inhomogeneous contrast that can impair clinical diagnosis (8).

Different methods for mitigating B_1^+ inhomogeneity have been proposed. Adiabatic pulses can excite a homogeneous flip angle distribution, because they are highly insensitive to the B_1^+ inhomogeneity (9). One example is the slice-selective adiabatic pulse using multiple subpulses in high-field MRI (10). Alternatively, spatially selective RF excitation techniques (11), such as the fast-k_z with five spokes (12) or the sparsity-enforced spokes placement algorithm (13), can be used to correct B_1^+ inhomogeneity. Simultaneous RF excitation from multiple RF coils with a fixed relative contribution but dynamic changes (14–18) can reduce B_1^+ inhomogeneities. Fully parallel transmission (pTx) techniques (19,20) can achieve the desired flip angle distribution with a shorter RF pulse than the spatially selective RF excitation method. In RF shimming, there is a common driving RF waveform, and only the amplitude and phase of each RF coil can be adjusted. pTx methods (13,21–25) provide more degrees of freedom for RF pulse design because they enable different RF waveforms being transmitted through each independent transmit coil element. Nonlinear spatial encoding magnetic fields (SEMs) have been used for selective magnetization excitation to reduce RF pulse length if the target excitation profile is a function of a linear combination of SEMs (26–31). Driving linear and quadratic SEMs between two excitation pulses can generate a spatially dependent transverse magnetization phase distribution that counteracts B_1^+ inhomogeneities to achieve a homogeneous flip angle distribution (32). Recently, we proposed the spatially selective excitation with generalized SEMs (SAGS) method to mitigate B_1^+ inhomogeneity, which enables the design of pulses in a lower dimensional k-space if isocontours of B_1^+ magnitude and isocontours of the designed SEM are geometrically similar (33).

[1]Institute of Biomedical Engineering, National Taiwan University, Taipei, Taiwan.
[2]Center for Advanced Imaging Innovation and Research and Bernard and Irene Schwartz Center for Biomedical Imaging, Department of Radiology, New York University School of Medicine, New York, New York, USA.
[3]Department of Neuroscience and Biomedical Engineering, Aalto University School of Science, Espoo, Finland

Grant sponsor: Taiwan Ministry of Science and Technology; Grant numbers: MOST 105-2221-E-002-104, MOST 104-2314-B-002-238, MOST 103-2628-B-002-002-MY3; Grant sponsor: Academy of Finland; Grant number: 298131; Grant sponsor: National Institutes of Health Center for Advanced Imaging Innovation and Research; Grant number: P41 EB017183.

*Correspondence to: Fa-Hsuan Lin, Ph.D., Institute of Biomedical Engineering, National Taiwan University, 1, Sec. 4, Roosevelt Road, Taipei 106, Taiwan. E-mail: fhlin@ntu.edu.tw

Received 15 April 2016; revised 5 August 2016; accepted 6 August 2016
DOI 10.1002/mrm.26397
Published online 00 Month 2016 in Wiley Online Library (wileyonlinelibrary.com).

In this study, we describe an alternative method to achieve homogeneous excitation using linear and nonlinear SEMs with RF shimming. By jointly designing SAGS and RF shimming, we are able to adjust both distributions of SEM and B_1^+ strength such that the distribution of B_1^+ strength can be approximated as a function of the distribution of SEM. This approximation allows efficient RF pulse design to achieve homogeneous excitation because of reduced k-space dimension in RF pulse design.

THEORY

SAGS

We previously proposed the SAGS method to achieve homogeneous excitation using a linear combination of the spatial distributions of the z-components of SEMs (33). Considering a two-dimensional slice-selective excitation scheme and using a spoke trajectory, the transverse magnetization magnitude $M_{xy}(x,y)$ on the x-y plane can be expressed as

$$M_{xy}(x,y) = \left| B_1^+(x,y) \sum_{s\in S} W(k_s) e^{2\pi j k_s h(x,y)} \right|, \quad [1]$$

Where $B_1^+(x,y)$ is the spatial distribution of the right-circularly polarized RF magnetic field transmitted by a volume coil, $W(k_s)$ is the RF pulse strength and phase at spoke location k_s, and $h(x,y)$ denotes the combined SEM. To achieve uniform transverse magnetization m_{xy}, we need to determine $W(k_s)$, k_s, and $h(x,y)$ such that $||m_{xy} - |B_1^+(x,y) \sum_{s\in S} W(k_s) e^{2\pi j k_s h(x,y)}||_2$ is minimized. The approximated optimal solution was found systematically in SAGS by first designing the $h(x,y)$ such that $|1/B_1^+(x,y)|$ can be approximated as a remapping of $h(x,y)$, and then determining $W(k_s)$ and k_s. In the original SAGS implementation, we only designed the $h(x,y)$ to fit an empirically measured $B_1^+(x,y)$ (33). For this study, we proposed that if we are not constrained to a predefined $B_1^+(x,y)$, we have more degrees of freedom in h(x,y) design, so we can find a remapping of $h(x, y)$ that matches $|1/B_1^+(x,y)|$ more closely. We considered this new approach as the jointly designed SAGS and RF shimming.

RF Shimming

In RF shimming, the B_1^+ fields of multiple RF coils are linearly combined to generate a net $B_{1\mathrm{shim}}^+(\mathrm{x},\mathrm{y},\xi)$:

$$B_{1shim}^+(x,y,\xi) = \left| \sum_{c=1}^{n_c} \xi_c B_1^c(x,y) \right| \quad [2]$$

Here, n_c denotes the number of RF coils. ξ_c and $B_1^c(x,y)$ are the complex modulation coefficient (i.e., amplitude and phase modulation) and the B_1^+ of the cth RF coil, respectively. ξ denotes the collections of all ξ_c's, $c = 1 \ldots n_c$. The transverse magnetization excited using RF shimming with a single RF pulse is

$$M_{xy}(x,y) = B_{1shim}^+(x,y,\xi) W(0). \quad [3]$$

In standard RF shimming, the coefficients ξ are typically chosen to achieve uniform flip angle distribution.

Jointly Designed SAGS and RF Shimming

The distribution of the excited transverse magnetization using jointly designed SAGS and RF shimming techniques is

$$M_{xy}(x,y) = \left| B_{1shim}^+(x,y,\xi) \sum_{s\in S} W(k_s) e^{2\pi j k_s h(x,y)} \right|. \quad [4]$$

Both $B_{1shim}^+(x,y,\xi)$ and $h(x,y)$ are unknown and are jointly designed by solving the optimization problem described next.

The Optimization Problem

Without losing generality, we assume that only SEMs of up to and including the second order are used in this study. Therefore, $h(x,y,\nu)$ denotes the magnetic field generated by the unknown combination of SEMs. ν denotes the unknown real-valued coefficients for combining SEMs. Its spatial distribution can be mathematically described using a quadratic polynomial:

$$h(x,y,\nu) = \sum_{q=0}^{2} \sum_{r=0}^{q} \nu_{q,r} x^r y^{q-r}. \quad [5]$$

The goal is to find ξ, ν, k_s, and $W(k_s)$ that minimize the squared error:

$$||m_{xy} - B_{1shim}^+(x,y,\xi)| \sum_{s\in S} W(k_s) e^{2\pi j k_s h(x,y,\nu)}||_2^2. \quad [6]$$

Note that m_{xy} is a real number, representing the targeted flip angle in a homogeneous excitation. An absolute value operator was used here, because we only aimed at achieving a uniform flip angle distribution without worrying about the phase distribution. This is a typical goal in mitigating B_1^+ inhomogeneity. However, the optimal solution is difficult to find, because the cost function is not convex. In order to simplify the optimization process, we only use spokes that are symmetrically located around the origin of k-space, with equal amplitudes and conjugate phases. Under this condition, $\sum_{s\in S} W(k_s) e^{2\pi j k_s h(x,y,\nu)}$ is real-valued, and Eq. 6 can be simplified as

$$||m_{xy} - B_{1shim}^+(x,y,\xi) \sum_{s\in S} W(k_s) e^{2\pi j k_s h(x,y,\nu)}||_2^2. \quad [7]$$

Note that we dropped the absolute value operator in Eq. 6 and considered only positive $\sum_{s\in S} W(k_s) e^{2\pi j k_s h(x,y,\nu)}$. For each negative $\sum_{s\in S} W(k_s) e^{2\pi j k_s h(x,y,\nu)}$, we can negate the sign of $W(k_s)$ such that $\sum_{s\in S} -W(k_s) e^{2\pi j k_s h(x,y,\nu)}$ is positive. Thus, if a negative $\sum_{s\in S} W(k_s) e^{2\pi j k_s h(x,y,\nu)}$ can minimize the cost, we should have found it as positive $\sum_{s\in S} -W(k_s) e^{2\pi j k_s h(x,y,\nu)}$. Note that such the solution $\{-W(k_s), k_s, h(x,y,\nu)\}$ was also within our search when we took positive $\sum_{s\in S} W(k_s) e^{2\pi j k_s h(x,y,\nu)}$. In summary, dropping the absolute value operator in Eq. 6 did not

matter for positive or negative $\sum_{s\in S} W(k_s)e^{2\pi jk_s h(x,y,\nu)}$. However, dropping the absolute value operator can be problematic when $\sum_{s\in S} W(k_s)e^{2\pi jk_s h(x,y,\nu)}$ includes both postive and negative values. In this case, the optimal solution includes postive, negative, and zero flip angles within the imaging object. Such a case was considered unlikely in practice and was therefore excluded in our calculation.

If we only use two spokes, the equation can be further simplified as

$$\begin{aligned}&||m_{xy} - B^{+}_{1shim}(x,y,\xi)2W(k_1)\cos(2\pi jk_1 h(x,y,\nu))||_2^2\\ &= ||m_{xy} - B^{+}_{1shim}(x,y,\xi)\sum_{s\in S} W(k_s)e^{2\pi jk_s h(x,y,\nu)}||_2^2.\end{aligned} \quad [8]$$

Both Eqs. 7 and 8 can be solved with the following two-step procedure. Note that the argument to the cosine term in Eq. 8 contained a constant ν_{00} (see Eq. 5), which enables the optimization to generate a sine flip angle distribution as well. We can also assume that $W(k_1)$ is a real-valued variable based on the same argument.

Step 1: Jointly Designed SEM and RF Shimming

Our previous work on SAGS suggested that 1) if $1/|B_1^+(x,y)|$ can be approximated by a remapping of $h(x,y)$, then the two-dimensional uniform excitation problem can be simplified to a one-dimensional excitation problem; 2) the flip angle homogeneity depends on the error between $1/|B_1^+(x,y)|$ and the remapping of $h(x,y)$. In the first step, we simultaneously optimize $\{\xi,\ \nu\}$ such that $1/B^{+}_{1shim}(x,y,\xi)$ can be approximated by a remapping of $h(x,y,\nu)$:

$$1/B^{+}_{1shim}(x,y,\xi) \approx D\Big(h(x,y,\nu)\Big). \quad [9]$$

Considering that $1/B^{+}_{1shim}(x,y,\xi)$ and $h(x,y,\nu)$ are both real-valued and smooth functions, we arbitrarily use a linear combination of the P^{th}-order harmonics to approximate $D(h)$:

$$D(h,\kappa,\rho) = \kappa_0 + \sum_{p=1}^{P}\Big(\kappa_p\cos(ph) + \rho_p\sin(ph)\Big). \quad [10]$$

With the above parametrization of D, the mapping problem (Eq. 9) can be formulated as an optimization problem aiming at adjusting parameters $\{\kappa,\rho,\xi,\nu\}$ to minimize the following error:

$$||1 - B^{+}_{1shim}(x,y,\xi)D(h(x,y,\nu),\kappa,\rho)||_2^2 \quad [11]$$

The algorithm for solving Eq. 11 is described in the Appendix. Note that the parameters $\{\kappa,\rho\}$ were nuisance parameters that were optimized for the choice of $\{\xi,\nu\}$ but discarded after the optimization. We also assumed function D is a cosine function for two spokes case as suggested by Eq. 8.

Step 2: Design of Spoke Locations and Associated RF Amplitudes and Phases

The optimized $\{\xi^{\text{opt}},\ \nu^{\text{opt}}\}$ yield $h(x,\ y,\nu^{\text{opt}})$ and $B^{+}_{1\text{shim}}(x,y,\xi^{\text{opt}})$. The goal of step 2 is to achieve a homogeneous flip angle m_{xy} using $2L$ spokes. We design the spoke locations (k^{opt}) in the k_h space, constraining them to be symmetrically distributed around the center of k-space, and the spoke amplitudes (W^{opt}) to achieve a homogeneous flip angle distribution.

$$\begin{aligned}&\{W^{opt}, k^{opt}\}\\ &= argmin_{\alpha,\beta}||m_{xy} - B^{+}_{1shim}(x,y,\xi^{opt})\sum_{l=-L,l\neq 0}^{L}\alpha_l e^{2\pi j\beta_l h(x,y,\nu^{opt})}||_2^2\\ &+ \lambda||\alpha||_2^2,\end{aligned} \quad [12]$$

where α_l was complex-valued.

In practice, we exhaustively search all possible spoke locations β_l, and the amplitudes α_l for these $2L$ spokes are determined by the least squared solution to Eq. 12. We added a regularization term $||\alpha_2^2||$ as a cost function to suppress solutions that require excessive RF power.

METHODS

Simulated B_1^+ Maps

A uniform sphere was modeled with dielectric constant $\varepsilon_r = 52$ and electric conductivity $\sigma = 0.55$ S/m to mimic the electrical properties of a human brain at 7 T. The full-wave electromagnetic field produced by a 20-element transmit array of identical circular coils uniformly packed around the sphere (diameter = 150 mm) was calculated using a semianalytical multipole expansion (34,35). For each coil element of the transmit array, we calculated the B_1^+ over a uniform grid of voxels (32×32) on a transverse field of view through the center of the sphere. All calculations were implemented using MATLAB (Mathworks, Natick, Massachusetts, USA) on a standard PC.

Experimental B_1^+ Maps

Phantom and in vivo B_1^+ maps were measured using a 7 T scanner (Magnetom, Siemens, Erlangen, Germany) equipped with an eight-channel pTX setup. The phantom had a spherical shape with 16.8 mm diameter and was filled with a doped saline solution (1.25 g of $NiS0_4 \times 6\,H_20$). A custom eight-element transceive head coil array was used (36). First, the actual flip angle imaging method (37) was used to obtain a quantitative B_1^+ map corresponding to the circular polarized (CP) mode (3 mm isotropic resolution, pulse repetition time $1/2 = 30/150$ ms, echo time = 1.5 ms, maximum flip angle $\pm 90^\circ$). Subsequently, a multislice fast low angle shot (FLASH) sequence was used to measure the relative signal amplitudes and phases corresponding to each of the individual channels and the CP mode (3 mm isotropic resolution, pulse repetition time = 500 ms, echo time = 2.0 ms, maximum flip angle = $\pm 10^\circ$). Finally, using the CP mode, one additional FLASH image was obtained with a longer echo time = 2.5 ms. Combining both CP mode FLASH images, a ΔB_0 was constructed. The quantitative B_1^+ maps corresponding to each of the individual transmit channels were derived as described previously (38). The same sequence parameters were used for both

phantom and in vivo measurements. One volunteer was examined with written informed consent in accordance with the regulations of our institute.

To reduce the noise in estimating the B_1^+ from the empirical data, we used a total variation denoising method (39). The RF shimming coefficients for generating a homogenous B_1^+ distribution were calculated based on the magnitude least squares method (23) using the CP mode as the initial guess. The computed RF shim was also denoised using total variation regularization.

Assessment of $|B_1^+|$ Inhomogeneity Mitigation

In all cases, we designed pulses to achieve a homogenous 10° flip angle distribution. In practice, we only searched the optimal solutions for two and four spokes located at conjugate locations. After optimizing pulse sequence design, the flip angle distribution was calculated based on the numerical solution of the Bloch equations. The performance in terms of achieved $|B_1^+|$ homogeneity was evaluated by calculating the relative standard deviation σ (32):

$$\sigma = \text{std}(M_{xy})/\text{mean}\ (M_{xy}), \qquad [13]$$

where std and mean represent the standard deviation and the mean of the transverse magnetization, respectively.

To evaluate excitation profile fidelity using the remapping of $h(x,y,\nu^{\text{opt}})$ to represent $1/B_{1shim}^+(x,y,\xi^{\text{opt}})$ we plotted the $(h(x,y,\nu^{\text{opt}}), 1/B_{1shim}^+(x,y,\xi^{\text{opt}}))$ pairs for all voxels. In the case of perfect remapping (Eq. 9), all pairs should be represented by one curve D(h). To quantify the accuracy of the remapping, we estimated a curve as

$$\text{a}_0 + \sum_{i=1}^{5}\left(a_i cos(ih) + b_i sin(ih)\right) \qquad [14]$$

based on all $(h(x,y,\nu^{\text{opt}}), 1/B_{1shim}^+(x,y,\xi^{\text{opt}}))$ pairs and calculated the errors between data pairs and the fitted curve. Where a_i, b_i are constants estimated by least squared fitting. The error was quantified as:

$$\text{std}(1/B_{1shim}{}^+(x,y,\xi^{\text{opt}}) - D(h(x,y,n^{\text{opt}})))/mean(D(h(x,y,n^{\text{opt}}))). \qquad [15]$$

Note that the optimized $h(x,y,\nu^{\text{opt}})$ is different between two-spoke (Eq. 8) and four-spoke (Eq. 7) excitation, because D is restricted to a cosine function in the two-spoke excitation. For comparison, we simulated the flip angle distribution obtained with the fast-k_z method, which used five spokes (12), and with SAGS using the standard RF (i.e., modulation coefficients designed to achieve a homogeneous $|B_1^+|$ distribution). Finally, we also simulated the flip angle distribution obtained by using jointly designed fast-k_z (with only linear SEMs) and RF shimming to investigate the differences between using nonlinear and linear SEMs.

To estimate the energy deposition associated with each method, for the simulated data we computed the global specific absorption rate (SAR) for each excitation (35). To make sure the number of spokes was sufficient in our algorithm, we simulated 99 equispaced spokes SAGS, which used the same $B_{1\text{shim}}^+(x,y)$ and $h(x,y,\nu^{\text{opt}})$ as in the jointly designed four-spoke SAGS and RF shimming. We also simulated the flip angle distribution of the jointly designed four-spoke SAGS and RF shimming using standard RF shim coefficients as the initial guess to investigate how the initial guess affects step 1 of the optimization.

RESULTS

Figure 1 shows the experimental B_1^+ maps of the brain and phantom measured at 7 T.

Figure 2 shows $|B_1^+|$ maps obtained with standard RF shimming aiming at maximizing homogeneity with jointly designed SAGS and RF shimming using two and four spokes and jointly designed fast-k_z and RF shimming for simulations, phantom experiments, and human head experiments. On visual inspection, standard RF shimming alone yielded relatively homogeneous $|B_1^+|$ distribution for both simulation and experimental data. The jointly designed SAGS and RF shimming and jointly designed fast-k_z and RF shimming both resulted in spatially inhomogeneous but smooth $|B_1^+|$ distributions. These asymmetric $B_{1\text{shim}}^+$ distributions were results of the optimization. We also found that the $|B_1^+|$ maps generated by the jointly designed fast-k_z and RF shimming method were significantly different from those in the other two cases. This was because 1) this $|B_1^+|$ distribution was able to generate a more homogeneous flip angle distribution by the numerical optimization and 2) fast-k_z can excite all flip angle distributions parameterized by $a_0 + \cos(a_1 x) + \cos(a_2 y)$ under a uniform B_1^+ (12), where a_0, a_1, and a_2 are arbitrary constants. Indeed, the numerical optimization revealed a B_1^+ distribution resembling a distribution with two peaks, which can counteract with the aforementioned parameterized flip angle distribution to achieve a homogeneous flip angle distribution.

One key requirement for our proposed method to generate a target (homogeneous) flip angle distribution is to find a remapping between $1/B_{1shim}{}^+(x,y,\xi^{\text{opt}})$ and $h(x,y,\nu^{\text{opt}})$ (Eq. 9). Figure 3 shows the distribution of $(1/B_{1shim}^+(x,y,\ \xi^{\text{opt}}), h(x,y,n^{\text{opt}}))$ pairs at all voxels in the imaging object. Ideally, in the case of perfect remapping, this distribution should be represented by one curve (Eq. 9). In practice, we estimated this curve by using a 10th-order polynomial (red curves in Fig. 3). Across simulations and experimental data, we found that the relation between $(1/B_{1shim}^+(x,y,\ \xi^{\text{opt}})$ and $h(x,y,\nu^{\text{opt}})$ is more closely described by a smooth one-dimensional function in jointly designed SAGS and RF shimming (Fig. 3, middle and bottom rows) than in standard RF shimming (Fig. 3, top row). In jointly designed SAGS and RF shimming, results with four spokes had more accurate remapping between $(1/B_{1shim}^+(x,y,\ \xi^{\text{opt}})$ and $h(x,y,\nu^{\text{opt}})$ than results with two spokes (note the reduced errors between the middle and bottom rows in Fig. 3). This is because different cost functions (two-spoke in Eq. 8 and four-spoke in Eq. 7) were used in the optimization. In particular, the two-spoke posed more stringent constraint by enforcing $(1/B_{1shim}^+(x,y,\ \xi^{\text{opt}})$ to be represented as a cosine function of h.

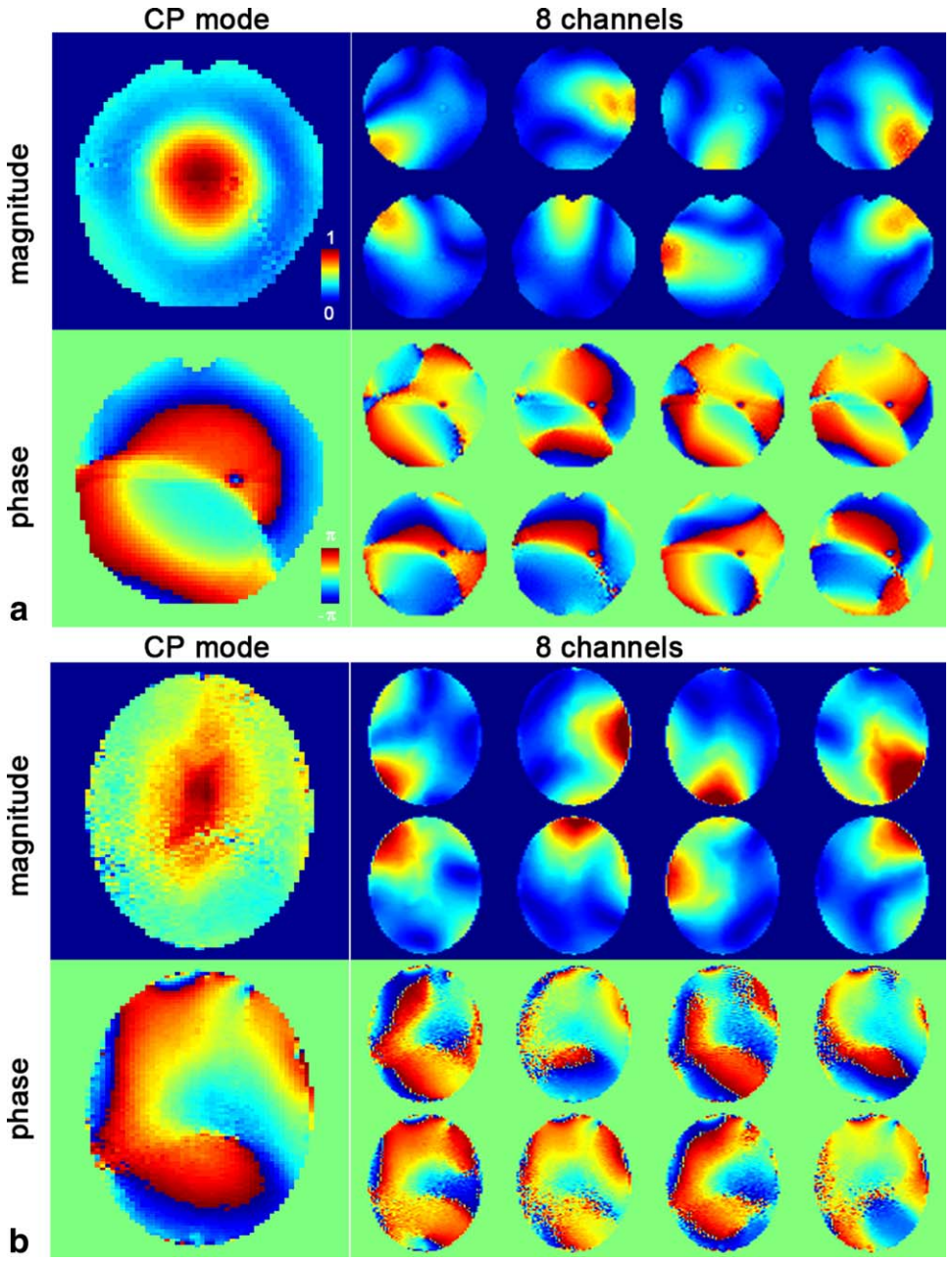

FIG. 1. (**A**) B_1^+ amplitude and phase maps of eight transmit channels and the CP mode combination in a saline phantom. (**B**) B_1^+ amplitude and phase maps of eight transmit channels and the CP mode combination in a human head.

Figure 4 shows the achieved flip angle distributions for all excitation methods. One-spoke excitation with standard RF shim generated a relatively homogeneous flip angle distribution (Fig. 4A), matching the $|B_1^+|$ distribution (first row in Fig. 2). The deviations from the target homogeneous flip angle distribution were $\sigma = 6.4\%$, 13.0%, and 13.2% for simulations, phantom, and human head experimental data, respectively. Fast-k_z applied with standard RF shim yielded $\sigma = 6.3\%$, 11.1%, and 11.0% for simulations, phantom, and human head experimental data, respectively (Fig. 4B). The SAGS method applied with standard RF shim yielded $\sigma = 6.2\%$, 10.7%, and 10.3% for simulations, phantom, and human head experimental data, respectively (Fig. 4C). Fast-k_z and SAGS applied with standard RF shim both show very similar excitation profile and only marginally improved the flip angle homogeneity compared with standard RF shimming alone.

The jointly designed SAGS and RF shimming generated flip angle distributions more homogeneous than standard RF shimming alone (Figs. 4D and 4E), even though the resulting B_1^+ distributions showed larger spatial variation (Fig. 2, second and third rows). In particular, using jointly designed SAGS and RF shimming with two spokes, the deviations from a perfectly homogeneous flip angle distribution were $\sigma = 2.8\%$, 9.3%, and 7.7% for simulations, phantom, and human head experimental data, respectively. Using four spokes, the error was instead $\sigma = 2.8\%$, 5.1%, and 6.2% for simulations, phantom, and human head experimental data, respectively. These results suggest that even if the B_1^+ distribution jointly designed using quadratic SEMs is

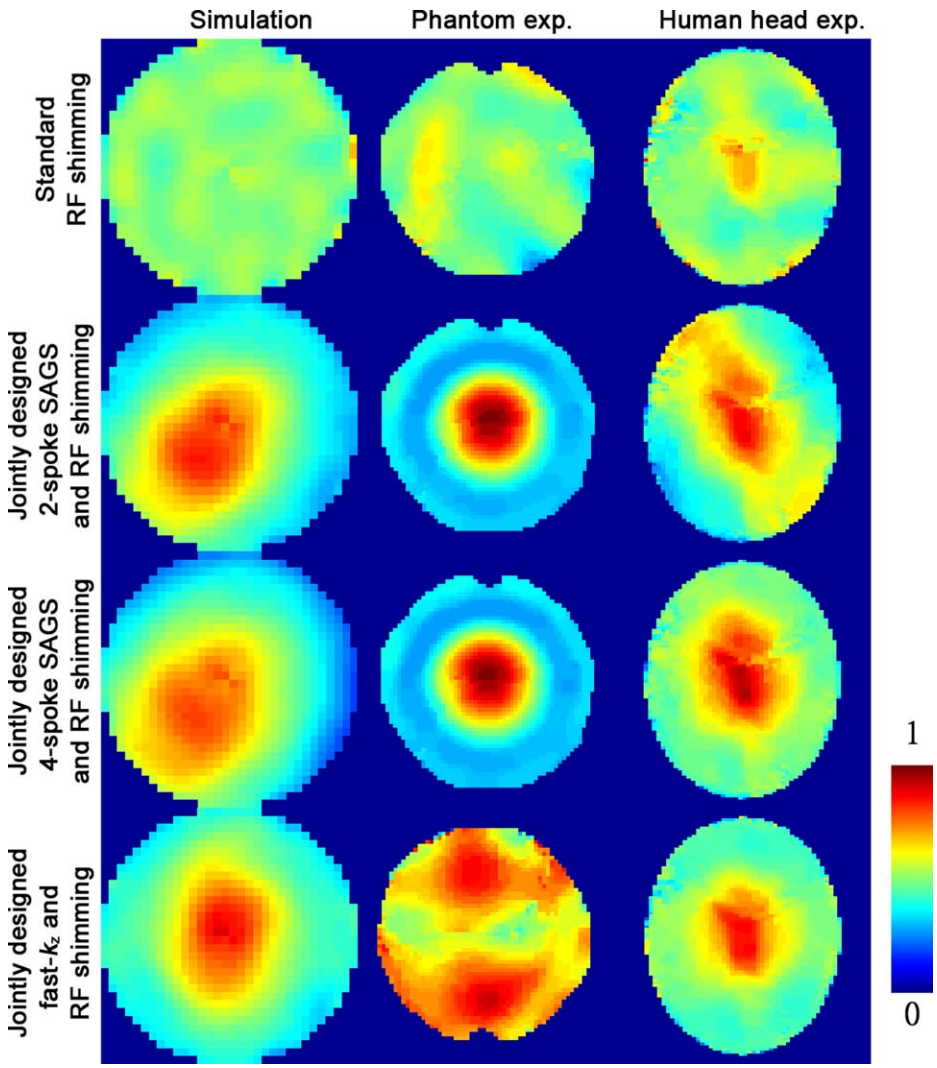

FIG. 2. $|B_1^+|$ maps obtained with standard RF shimming aiming at achieving the maximal homogeneity (first row), jointly designed SAGS and RF shimming with two spokes (second row) and four spokes (third row), and jointly designed fast-k_z and RF shimming (fourth row) for simulations (left column), phantom experiments (middle column), and human head experiments (right column).

inhomogeneous, it can still achieve a homogeneous flip angle distribution. Figure 4F shows the flip angle distribution using the $B_{1\text{shim}}^+$ obtained from the jointly designed SAGS and RF shimming with 99 equally spaced spokes. The results were similar to those with four spokes, suggesting that the number of spokes, after careful tuning of spoke locations, amplitudes, and phases, is not the bottleneck for further improving the flip angle homogeneity. Figure 4G shows that jointly designed fast-k_z and RF shimming with five spokes generated a more homogeneous flip angle distribution than the fast-k_z applied with standard RF shim, with $\sigma = 3.8\%$, 9.4%, and 8.1% for simulations, phantom, and human head experimental data, respectively. This result supports the use of a joint design approach. SAR and homogeneity for simulation data are summarized in Table 1. Note that the SAR associated with the fast-k_z method using standard RF shim was very similar to the SAR of standard RF shimming alone. In fact, the side spokes of fast-k_z had a minimal contribution to improving the homogeneity of the flip angle distribution and the center spoke had similar amplitude than the single spoke excitation of standard RF shimming. In particular, the amplitude of side spokes along k_x and k_y axes were 0.9% and 0.1% of the center spoke, respectively.

The initial guess for $(1/B_{1shim}^+(x, y, \xi^{\text{opt}})$ in the calculations for Figures 2 and 4 was chosen to be the CP mode of the combination of all transmit coils. We repeated the simulations using the result from standard RF shimming as the initial guess to test the stability of our method. We found that the results of the jointly designed SAGS and RF shimming with four spokes were not sensitive to the initial guess for $(1/B_{1shim}^+(x, y, \xi^{\text{opt}})$, as shown by the similarity between Figure 5 and Figure 4E.

DISCUSSION

We proposed a joint design method to improve flip angle homogeneity by optimizing the combination of nonlinear SEMs and RF shimming concurrently. In our previous SAGS approach, we clearly demonstrated the advantage of establishing a remapping between a given B_1^+ and a combined SEM in simplifying the pulse design in a lower dimensional k-space when the goal is to achieve a homogenous flip angle distribution (33). The current study further extends this advantage to encompass RF

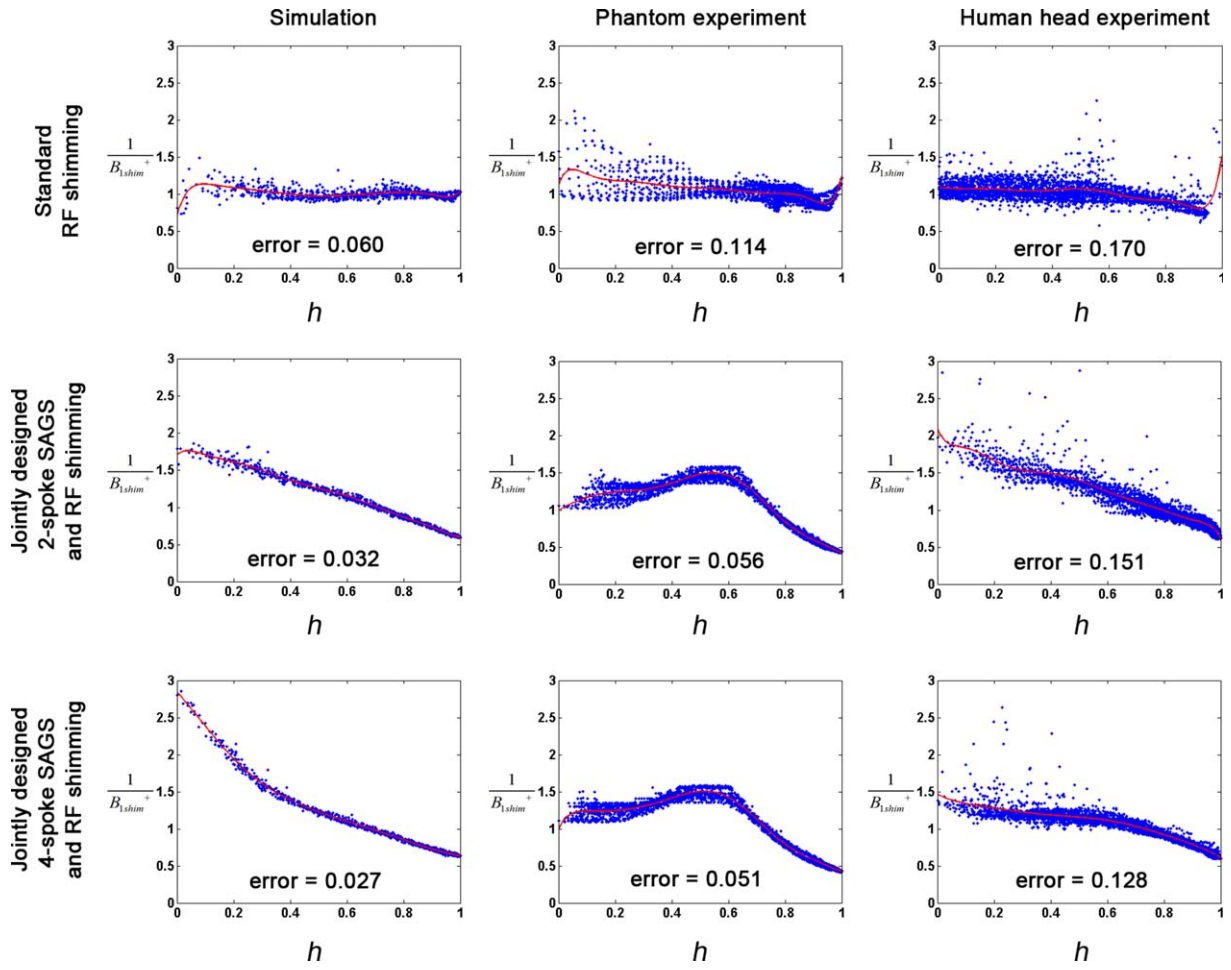

FIG. 3. The relationship between $h(x,y)$ and $1/B_{1\text{shim}}^{+}(x,y)$ in standard RF shimming (top row) and jointly designed SAGS and RF shimming with two spokes (second row) or four spokes (bottom row) using simulations, experimental saline phantom data, and experimental human head data. The mapping error quantified by the root mean square of the residuals between $(h(x,y), 1/B_{1\text{shim}}^{+}(x,y))$ pairs and a fitted curve using 10th-order polynomials is reported for each plot.

shimming. Specifically, we used both simulated and experimentally measured data to demonstrate the benefits of using linear and quadratic SEMs to achieve a better remapping between a B_1^+ and SEM combination. This better remapping also led to improved flip angle distribution homogeneity (Fig. 4). We showed that our proposed jointly designed SAGS and RF shimming approach with four spokes can improve flip angle homogeneity by more than 50% compared with standard RF shimming.

Our results support the importance of optimizing the combination of transmit coils (RF shimming) while simultaneously tailoring the combinations of linear and nonlinear SEMs. The simplest approach would be to first use standard RF shimming to search for the optimal complex-valued coil combination coefficients that achieve a homogeneous B_1^+ distribution (14) and then adjust the combination of linear and nonlinear SEMs such that B_1^+ can be approximated as a remapping of the SEM. However, our results showed that such sequential approach is suboptimal (Fig. 4C) compared with designing RF shimming and adjusting the combination of SEMs simultaneously (Fig. 4E).

The proposed approach currently has two limitations, which are related to 1) the accuracy of the remapping (Eq. 9) and 2) the use of a finite number of spokes to engineer the desired flip angle distribution (Eq. 12). However, Figures 4E and 4F shows that flip angle homogeneity was similar between the results using 99 equally spaced spokes and the results using four tailored spokes. This result suggests that the number of spokes was not the bottleneck in improving the flip angle homogeneity, but rather that the accuracy of the remapping between the B_1^+ and the SEM is the key to achieving the ultimate flip angle distribution. In fact, we observed that a smaller fitting error in Figure 3 generally corresponded to a more homogeneous flip angle distribution in Figure 4.

In the ideal case of homogeneous B_1^+, RF excitation using linear or nonlinear SEM can produce different flip angle excitation at locations with different SEM magnitudes of SEM. This suggests the that an inhomogeneous flip angle distribution can be carefully crafted to counteract an inhomogeous B_1^+ distribution, such that a homogeneous flip angle distribution is created. These were indeed the cases in Figures 4D and 4E.

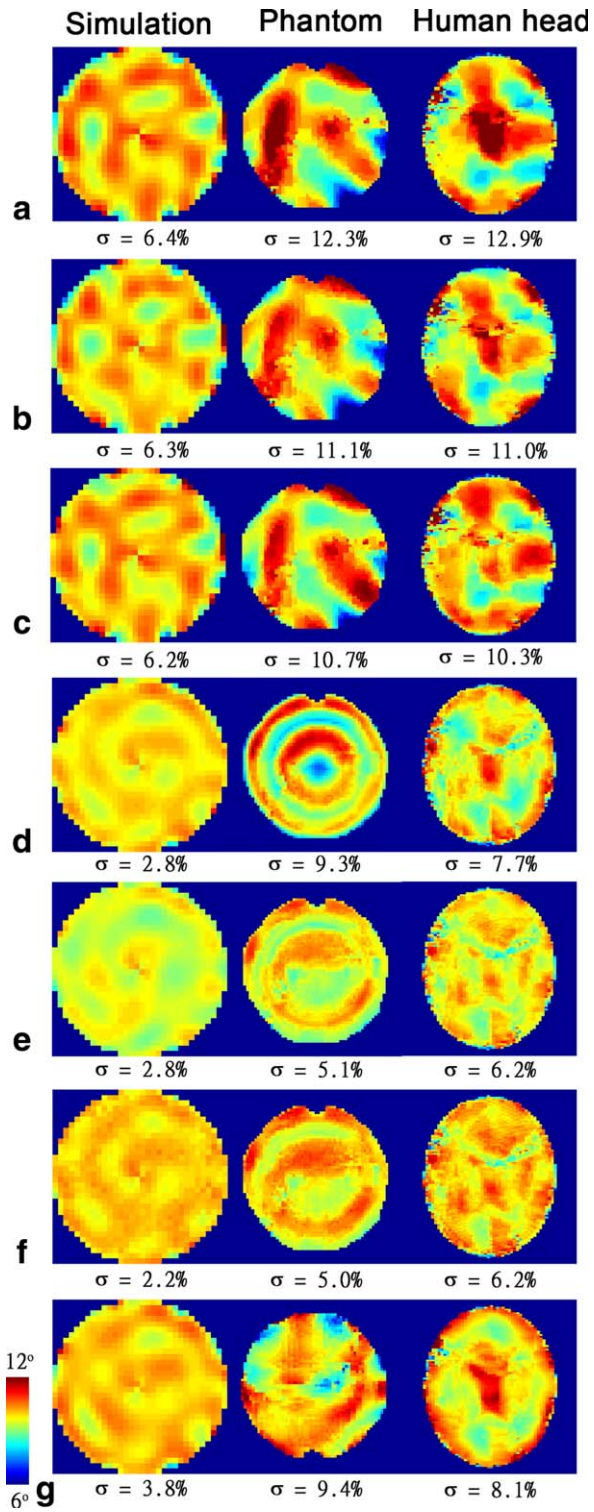

FIG. 4. Flip angle distributions. (**A**) One spoke excitation with standard RF shim. (**B**) Five spokes fast-k_z with standard RF shim. (**C**) SAGS with standard RF shim and four spokes. (**D**) Jointly designed SAGS and RF shimming with two spokes. (**E**) Jointly designed SAGS and RF shimming with four spokes. (**F**) Jointly designed SAGS and RF shimming with 99 equally spaced spokes. (**G**) Jointly designed fast-k_z and RF shimming with five spokes. Simulations, experimental saline phantom data, and experimental human head data are shown in the left, middle, and right columns, respectively. The relative standard deviation σ is reported below each map.

We envision two potential methods that could further decrease the remapping error. One possibility is to use more transmit coils in order to increase the degrees of freedom of RF shimming. The other possibility is to use more nonlinear SEMs. Specifically, we may consider either higher than the 2nd-order SEMs (40) or localized SEMs (41), such that the optimal iso-intensity of B_{1shim}^{+} in our method is no longer restricted to conic. However, experimental results are needed to validate such speculation.

Note that the combination of pTx and nonlinear SEMs has been reported to effectively produce a homogeneous flip angle distribution (42). Our proposed method, however, is different from the combination of pTx and nonlinear SEMs (42). First, like RF shimming, we only need one common driving RF exciter to implement the RF pulse using a vector modulator to deliver the same waveform with varying amplitudes and phases for each transmit coil (43); thus, the complexity and the cost are expected to be less than a pTx with a nonlinear SEM system. Second, the pulse sequence involving nonlinear SEMs is typically designed on a multidimensional k-space, whose dimension equals the number of SEMs. Jointly designed SAGS and RF shimming is one method to reduce design complexity with a reduced k-space dimension. The benefit of such dimension reduction has been reported in our previous work (33).

Although our results seem promising, the practical limitation of our method is the need of quadratic SEMs, which are not widely accessible yet. The other potential challenge of our method is the need for accurate phase and magnitude B_1^+ maps for the individual transmit coils. In the final step of our algorithm, we search all possible spokes locations exhaustively. This approach is computationally possible when only a few spokes are used (the search for two and four spokes in this work required less than 5 s) because the computational time is linearly proportional to the number of combinations of all possible spoke locations. Specifically, the computation time would become $T^{n/2}$ for n-spoke if time T was spent in searching for a two-spoke solution. In order to use a large number of spokes, the combination of greedy type methods and gradient descent methods could be a more efficient approach to optimize the position of the spokes (44).

Table 1
Relative SAR and Flip Angle Homogeneity (σ) of Different Methods Using Simulation Data

Method	Relative SAR	Homogeneity (σ)
Standard RF shim	1.00	6.4%
Fast-k_z + standard RF shim	1.00	6.3%
SAGS + standard RF shim with four spokes	0.48	6.2%
Jointly designed SAGS and RF shimming with two spokes	2.56	2.8%
Jointly designed SAGS and RF shimming with four spokes	11.16	2.8%
Jointly designed fast-k_z and RF shimming	6.62	3.8%

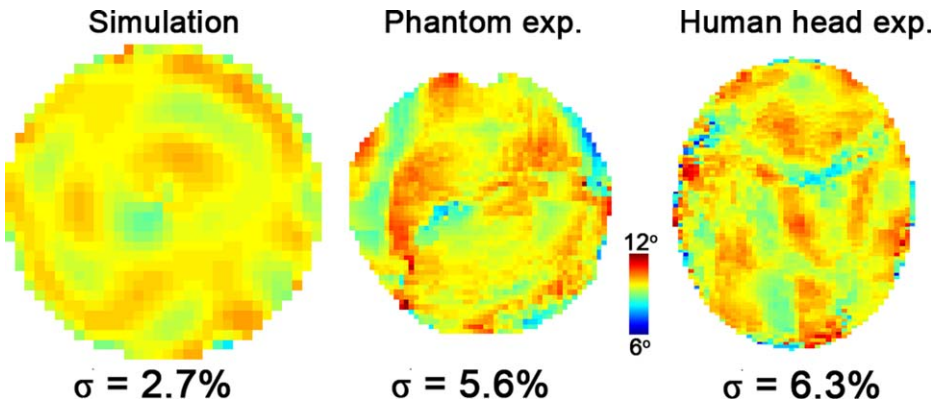

FIG. 5. Flip angle distribution maps generated by jointly designed SAGS and RF shimming with four spokes with B^{+}_{1shim} optimized for a homogeneous flip angle as the initial guess. The relative standard deviation σ is reported below each plot.

In this study, we restricted the spoke locations to be symmetrically located around the center of *k*-space, for the sake of computation efficiency. If spoke locations, β, are symmetric (conjugated), spoke coefficients are automatically conjugated, because $B^{+}_{1shim}(x,y)$ was defined to be real. In this case, we can solve α efficiently by least squares fitting (Eq. 12). Naturally, allowing spokes with arbitrary locations, amplitudes, and phases can improve the results by increasing the degrees of freedom of pulse design at the cost of higher complexity in the optimization. Note, however, that even when using four spokes with the restriction of conjugated spoke locations and equal amplitudes, we were able to achieve a relatively homogeneous flip angle distribution compared with the test case with 99 spokes (Figs. 4E and 4F). Therefore, we expect minimal improvement in flip angle homogeneity by using more spokes or without restricting spoke locations.

Equation 12 excluded $\ell = 0$, because this spoke ($\ell = 0$) only contributes to a constant flip angle, which is not very useful in counteracting an inhomogeneous B^{+}_{1}. Furthermore, using an even number ($2n$) of spokes can also produce any possible excitation distribution using $2n$-1 spokes. This is because when two central spokes are very close to 0 (*k*-space center), the result is equivalent to the case of using $2n$-1 spokes. Based on these two reasons, we did not include the $\ell = 0$ term in our calculation.

The same strategy of jointly designed SAGS and RF shimming may be applied to uniform three-dimensional excitation if good remapping exists between the RF shim and the SEM. However, we expect that the remapping error may be significant limiting the performance of this method in achieving a homogeneous volumetric flip angle distribution.

Table 1 shows that the relative SAR was lower for the jointly designed SAGS and RF shimming with two spokes than for the jointly designed SAGS and RF shimming with four spokes, whereas the homogeneity of the two solutions was nearly identical. This is likely due to the fact that an SAR minimization constraint was not included in the design of the B^{+}_{1shim} and h (Eq. 11). Including SAR minimization in the pulse design is expected to increase the complexity of the optimization.

One clear disadvantage of our method is a higher SAR (Table 1) compared with standard RF shimming. This is the consequence of seeking a homogeneous flip angle distribution in the RF shimming step. Because there is a trade-off between M_{xy} homogeneity and SAR (32), we expect that modifying our pulse design, for example, to allow less extreme B^{+}_{1} values with conic iso-intensity contours, could reduce SAR at the cost of flip angle homogeneity. Additionally, we may impose local SAR constraints by using virtual observation points to jointly design other pulses with lower SAR. Further investigation is required to validate these hypotheses.

In conclusion, we proposed a jointly designed SAGS and RF shimming approach to mitigate B^{+}_{1} inhomogeneity, a prominent artifact in high-field imaging. Our simulations and experimental results suggest that this approach could facilitate structural and functional imaging at ultra high-field MRI.

APPENDIX: ALGORITHM FOR MINIMIZING EQ. 11

Initializing Parameters

Our chosen initial guess for ξ^{old} was the combination of CP mode (43), and the initial guess for κ^{old} and ρ^{old} was zero except $\kappa_1^{old} = \max_{x,y}(1/B^{+}_{1shim}(x,y,\xi))$.

$$\nu^{old} = argmin_{\nu}||\sum_{q=0}^{2}\sum_{r=0}^{1}\nu_{q,r}(x^r y^{q-r}) - \arccos\frac{B^{+}_{1shim}(x,y,\xi)}{\kappa_1}||_2^2 \quad [A1]$$

Iterative Updating

Using a combination of the gradient descent algorithm and least squares solution iteratively, we adjusted {κ, ρ, ξ, ν} to minimize

$$\Phi\left(\kappa,\rho,\xi,\nu,B^{+}_{1phase}(x,y,\xi)\right) = ||e^{iB^{+}_{1phase}(x,y,\xi)} - \sum_{c=1}^{n_c}\xi_c B_1^c(x,y)D(h(x,y,\nu),\kappa,\rho)||_2^2, \quad [A2]$$

where $B^{+}_{1phase}(x,y,\xi)$ represents the phase distribution of $\sum_{c=1}^{n_c}\xi_c B_1^c(x,y)$. Allowing $B^{+}_{1phase}(x,y,\xi)$ as a free parameter in the optimization is equivalent to using a least squares magnitude design to relax the phase constraint on the desired excitation profile.

Step 1

With given $\kappa^{\text{old}}, \rho^{\text{old}}, \xi^{\text{old}}, \nu^{\text{old}}, B_{1phase}^{+}(x,y,\xi^{\text{old}})$, we updated the value of ν using the gradient descent algorithm with the step size λ,

$$\nu^{\text{new}} = \nu^{old} - \lambda\nabla_{\nu}\Phi \quad [A3]$$

Step 2

We used the least squares algorithm to find the κ^{new} and σ^{new}:

$$\{\kappa^{\text{new}}, \rho^{\text{new}}\} = \underset{\kappa,\rho}{\operatorname{argmin}}\,\Phi\left(\kappa, \rho, \xi^{\text{old}}, \nu^{\text{new}}, B_{1phase}^{+}(x,y,\xi^{\text{old}})\right) \quad [A4]$$

Step 3

We used a least squares algorithm to find the new ξ:

$$\xi^{new} = \underset{\kappa,\sigma}{\operatorname{argmin}}\,\Phi\left(\kappa^{\text{new}}, \rho^{\text{new}}, \xi^{\text{old}}, \nu^{\text{new}}, B_{1phase}^{+}(x,y,\xi^{\text{old}})\right) \quad [A5]$$

We repeated steps 1–3 until the cost converged:

$$\Phi\left(\kappa^{\text{old}}, \rho^{\text{old}}, \xi^{\text{old}}, \nu^{\text{old}}, B_{1phase}^{+}(x,y,\xi^{\text{old}})\right) - \Phi\left(\kappa^{\text{new}}, \rho^{\text{new}}, \xi^{\text{new}}, \nu^{\text{new}}, B_{1phase}^{+}(x,y,\xi^{\text{new}})\right) < \epsilon \quad [A6]$$

When not converging, we updated $\kappa^{\text{old}}, \rho^{\text{old}}, \xi^{\text{old}}, \nu^{\text{old}} \leftarrow \kappa^{\text{new}}, \rho^{\text{new}}, \xi^{\text{new}}, \nu^{\text{new}}$ and repeated steps 1–3. At convergence, we obtained the optimized parameters $\kappa^{\text{opt}}, \rho^{\text{opt}}, \xi^{\text{opt}}, \nu^{\text{opt}} \leftarrow \kappa^{\text{new}}, \rho^{\text{new}}, \xi^{\text{new}}, \nu^{\text{new}}$.

REFERENCES

1. Hoult D, Richards R. The signal to noise ratio of the nuclear magnetic resonance experiment. J Magn Reson 1976;24:71–85.
2. de Graaf RA, Brown PB, McIntyre S, Nixon TW, Behar KL, Rothman DL. High magnetic field water and metabolite proton T1 and T2 relaxation in rat brain in vivo. Magn Reson Med 2006;56:386–394.
3. Yacoub E, Shmuel A, Pfeuffer J, Van De Moortele PF, Adriany G, Ugurbil K, Hu X. Investigation of the initial dip in fMRI at 7 Tesla. NMR Biomed 2001;14:408–412.
4. Ibrahim TS, Lee R, Abduljalil AM, Baertlein BA, Robitaille PML. Dielectric resonances and B-1 field inhomogeneity in UHFMRI: computational analysis and experimental findings. Magn Reson Imag 2001;19:219–226.
5. Bernstein MA, Huston J 3rd, Ward HA. Imaging artifacts at 3.0T. J Magn Reson Imag 2006;24:735–746.
6. Franklin KM, Dale BM, Merkle EM. Improvement in B1-inhomogeneity artifacts in the abdomen at 3T MR imaging using a radiofrequency cushion. J Magn Reson Imag 2008;27:1443–1447.
7. Vaughan JT, Garwood M, Collins CM, et al. 7T vs. 4T: RF power, homogeneity, and signal-to-noise comparison in head images. Magn Reson Med 2001;46:24–30.
8. Marques JP, Kober T, Krueger G, van der Zwaag W, Van de Moortele PF, Gruetter R. MP2RAGE, a self bias-field corrected sequence for improved segmentation and T1-mapping at high field. NeuroImage 2010;49:1271–1281.
9. Tannus A, Garwood M. Adiabatic pulses. NMR Biomed 1997;10:423–434.
10. Balchandani P, Glover G, Pauly J, Spielman D. Improved slice-selective adiabatic excitation. Magn Reson Med 2014;71:75–82.
11. Pauly JM, Nishimura DG, Macovski A. A k-space analysis of small-tip-angle excitation. J Magn Reson 1989;81:43–56.
12. Saekho S, Yip CY, Noll DC, Boada FE, Stenger VA. Fast-kz three-dimensional tailored radiofrequency pulse for reduced B1 inhomogeneity. Magn Reson Med 2006;55:719–724.
13. Zelinski AC, Wald LL, Setsompop K, Alagappan V, Gagoski BA, Goyal VK, Adalsteinsson E. Fast slice-selective radio-frequency excitation pulses for mitigating B_1^+ inhomogeneity in the human brain at 7 Tesla. Magn Reson Med 2008;59:1355–1364.
14. Ibrahim TS, Lee R, Baertlein BA, Abduljalil AM, Zhu H, Robitaille PM. Effect of RF coil excitation on field inhomogeneity at ultra high fields: a field optimized TEM resonator. Magn Reson Imaging 2001; 19:1339–1347.
15. Mao W, Smith MB, Collins CM. Exploring the limits of RF shimming for high-field MRI of the human head. Magn Reson Med 2006;56: 918–922.
16. Collins CM, Liu W, Swift BJ, Smith MB. Combination of optimized transmit arrays and some receive array reconstruction methods can yield homogeneous images at very high frequencies. Magn Reson Med 2005;54:1327–1332.
17. Vaughan T, DelaBarre L, Snyder C, et al. 9.4T human MRI: preliminary results. Magn Reson Med 2006;56:1274–1282.
18. Metzger GJ, Snyder C, Akgun C, Vaughan T, Ugurbil K, Van de Moortele PF. Local B1 + shimming for prostate imaging with transceiver arrays at 7T based on subject-dependent transmit phase measurements. Magn Reson Med 2008;59:396–409.
19. Katscher U, Bornert P, Leussler C, van den Brink JS. Transmit SENSE. Magn Reson Med 2003;49:144–150.
20. Zhu Y. Parallel excitation with an array of transmit coils. Magn Reson Med 2004;51:775–784.
21. Grissom W, Yip CY, Zhang Z, Stenger VA, Fessler JA, Noll DC. Spatial domain method for the design of RF pulses in multicoil parallel excitation. Magn Reson Med 2006;56:620–629.
22. Setsompop K, Alagappan V, Gagoski BA, Potthast A, Hebrank F, Fontius U, Schmitt F, Wald LL, Adalsteinsson E. Broadband slab selection with B1 + mitigation at 7T via parallel spectral-spatial excitation. Magn Reson Med 2009;61:493–500.
23. Setsompop K, Wald LL, Alagappan V, Gagoski BA, Adalsteinsson E. Magnitude least squares optimization for parallel radio frequency excitation design demonstrated at 7 Tesla with eight channels. Magn Reson Med 2008;59:908–915.
24. Setsompop K, Wald LL, Alagappan V, Gagoski B, Hebrank F, Fontius U, Schmitt F, Adalsteinsson E. Parallel RF transmission with eight channels at 3 Tesla. Magn Reson Med 2006;56:1163–1171.
25. Wu X, Schmitter S, Auerbach EJ, Moeller S, Ugurbil K, Van de Moortele PF. Simultaneous multislice multiband parallel radiofrequency excitation with independent slice-specific transmit B1 homogenization. Magn Reson Med 2013;70:630–638.
26. Weber H, Gallichan D, Schultz G, Witschey WR, Welz AM, Cocosco CA, Hennig J, Zaitsev M. ExLoc: Excitation and Encoding of Curved Slices. In Proceedings of the 19th Annual Meeting of ISMRM, Montreal, Quebec, Canada, 2011. p. 2806.
27. Haas M, Ullmann P, Schneider JT, Ruhm W, Hennig J, Zaitsev M. Large Tip Angle Parallel Excitation Using Nonlinear Non-bijective PatLoc Encoding Felds. In Proceedings of the 18th Annual Meeting of ISMRM, Stockholm, Sweden, 2010. p. 4929.
28. Schneider JT, Haas M, Ohrel S, Lehr H, Ruhm W, Post H, Hennig J, Ullmann P. Parallel Spatially Selective Excitation Using Nonlinear Non-bijective Patloc Encoding Fields: Experimental Realization and First Results. In Proceedings of the 19th Annual Meeting of ISMRM, Montreal, Quebec, Canada, 2011. p. 211.
29. Ma C, Xu D, King KF, Liang ZP. Reduced field-of-view excitation using second-order gradients and spatial-spectral radiofrequency pulses. Magn Reson Med 2013;69:503–508.
30. Kopanoglu E, Yilmaz U, Gokhalk Y, Atalar E. Specific absorption rate reduction using nonlinear gradient fields. Magn Reson Med 2013;70: 537–546.
31. Haas M, Ullmann P, Schneider JT, Post H, Ruhm W, Hennig J, Zaitsev M. PexLoc-parallel excitation using local encoding magnetic fields with nonlinear and nonbijective spatial profiles. Magn Reson Med 2013;70:1220–1228.
32. Duan Q, van Gelderen P, Duyn J. Tailored excitation using nonlinear B0-shims. Magn Reson Med 2012;67:601–608.
33. Hsu YC, Chern IL, Zhao W, Gagoski B, Witzel T, Lin FH. Mitigate B1 (+) inhomogeneity using spatially selective radiofrequency excitation with generalized spatial encoding magnetic fields. Magn Reson Med 2014;71:1458–1469.

34. Keltner JR, Carlson JW, Roos MS, Wong ST, Wong TL, Budinger TF. Electromagnetic fields of surface coil in vivo NMR at high frequencies. Magn Reson Med 1991;22:467–480.
35. Lattanzi R, Sodickson DK, Grant AK, Zhu Y. Electrodynamic constraints on homogeneity and radiofrequency power deposition in multiple coil excitations. Magn Reson Med 2009;61:315–334.
36. Wiggins GC, Zhang B, Chen G, Sodickson DK. A Highly Decoupled 8 Channel Transmit-Receive Loop Array for 7T with Diverse B1 Profiles. In Proceedings of the 20th Annual Meeting of ISMRM, Melbourne, Victoria, Australia, 2012. p. 309.
37. Yarnykh VL. Actual flip-angle imaging in the pulsed steady state: a method for rapid three-dimensional mapping of the transmitted radiofrequency field. Magnet Reson Med 2007;57:192–200.
38. Van de Moortele PF, Snyder C, DelaBarre L, Adriany G, Vaughan T, Ugurbil K. Calibration Tools for RF Shim at Very High Field with Multiple Element RF Coils: From Ultra Fast Local Relative Phase to Absolute Magnitude B1 + Mapping. In Proceedings of the 15th Annual Meeting of ISMRM, Berlin, Germany, 2007. p. 1676.
39. Rudin LI, Osher S, Fatemi E. Nonlinear total variation based noise removal algorithms. Physica D 1992;60:259–268.
40. Kim DH, Adalsteinsson E, Glover GH, Spielman DM. Regularized higher-order in vivo shimming. Magn Reson Med 2002;48:715–722.
41. Hsu JJ, Glover GH. Mitigation of susceptibility-induced signal loss in neuroimaging using localized shim coils. Magn Reson Med 2005;53:243–248.
42. Grissom WA, Sacolick L, Vogel MW. B_1^+ Inhomogeneity Compensation Using 3D Parallel Excitation Is Enhanced by Simultaneous Linear and Nonlinear Gradient Encoding. In Proceedings of the 19th Annual Meeting of ISMRM, Montreal, Quebec, Canada, 2011. p. 2898.
43. Yazdanbakhsh P, Solbach K, Bitz AK. Variable power combiner for RF mode shimming in 7-T MR imaging. IEEE T Bio-Med Eng 2012;59:2549–2557.
44. Grissom WA, Khalighi MM, Sacolick LI, Rutt BK, Vogel MW. Small-tip-angle spokes pulse design using interleaved greedy and local optimization methods. Magn Reson Med 2012;68:1553–1562.